Korean J. Chem. Eng., 36(2), 312-320 (2019)
DOI: 10.1007/s11814-018-0199-1

pISSN: 0256-1115
eISSN: 1975-7220

Mesoporous carbon nanofiber engineered for improved supercapacitor performance

Subrata Ghosh*,‡, Wan Dao Yong*,‡, En Mei Jin*,†, Shyamal Rao Polaki, Sang Mun Jeong*,†, and Hangbae Jun*****

*Department of Chemical Engineering, Chungbuk National University, Chungbuk 28644, Korea
**Surface and Nanoscience Division, Materials Science Group, Indira Gandhi Centre for Atomic Research, Homi Bhabha National Institute, Kalpakkam, Tamil Nadu- 603102, India
***Department of Environmental Engineering, Chungbuk National University, Chungbuk 28644, Korea
(*Received 16 October 2018 • accepted 25 November 2018*)

Abstract−Carbon nanofiber is a well-known carbon nanostructure employed in flexible supercapacitor electrode. Despite recent developments, improvement in the performance of carbon nanofiber-based electrode is still the subject of intense research. We investigated the supercapacitor performance of porosity-induced carbon nanofibers (CNFs). The fabrication process involves electrospinning, calcination, and subsequent etching. The porous CNF not only delivers a higher capacitance of 248 F/g at a current density of 1 A/g, but also exhibits a higher rate performance of 73.54%, lower charge transfer resistance and only 1.1% capacitance loss after 2000 charge-discharge cycles, compared to pristine CNF. The excellent electrochemical behavior of porous CNF is correlated with the degree of graphitization, a higher volume of mesopores, and enhanced surface area. The as-fabricated symmetric device comprising porous CNF exhibits an energy density of 9.9 Wh/kg, the power density of 0.69 kW/kg and capacitance retention of 89% after 5000 charge-discharge cycles. The introduction of porosity in CNFs is a promising strategy to achieve high-performance supercapacitor electrode.

Keywords: Supercapacitor, Porous Carbon Nanofiber, Electrospinning, Specific Capacitance, Tandem Cell

INTRODUCTION

Electrochemical capacitors or supercapacitors are promising candidates to replace traditional energy storage devices [1,2]. With their high power density, prolonged cycle life, and moderate energy density, supercapacitors can be employed in various applications, including hybrid electric vehicles, memory backups, and power grids. However, the complete utilization of supercapacitors as an independent energy device is limited by their energy density. Supercapacitor devices typically consist of two electrodes separated by an electrolyte-soaked separator. Hence, their energy density can be improved by developing novel materials with excellent physic-chemical properties and electrolytes that can fully penetrate the material at high operating voltages [3-8]. Carbon-based materials have been extensively studied as electrode materials owing to their excellent conductivity, stability, and high surface area [5,9,10]. Charge storage in such materials is enabled by the formation of a double layer across the electrode/electrolyte interface. Considering their advantages, enhancing the energy density of carbon-based supercapacitors is of immense technological concern [8,11,12].

Carbon nanofibers (CNFs) are a highly promising supercapacitor electrode material owing to their unique structure, high surface area, flexibility, and electronic conductivity [13-16]. In addition, CNFs are suitable as platforms to grow heterostructures for high-performance supercapacitor applications [17-21]. Thus far, the specific capacitance of CNFs has been limited to ~200 F/g despite intensive research efforts [13,22]; this is true even for structures other than carbon nanostructures [1]. Generally, CNFs are prepared by template methods and electrospinning [13,21-24]. CNF prepared by a combination of hard-templating and soft-templating methods yielded a maximum capacitance of only 167 F/g [23]. The supercapacitive properties of electrospun CNFs can be tuned easily by controlling its diameter and porosity via electrospinning [13,21]. However, the rate performance and poor electronic conductivity of electrospun CNF-based electrodes are of prime concern [22,24]. Metal-ion assisted corrosion enabled the production of porous CNF that exhibited the highest capacitance of 104 F/g at 0.2 A/g [25]. The interface miscibility-induced approach is another promising approach adopted to construct double-capillary carbon nanofibers (DCNFs) with micropores in the inner capillary and mesopores in the outer capillary. This unique structure achieves synergism between high accessibility to the electrolyte, a short diffusion length for ions, high conductivity, and high flexibility. DCNFs can be directly used as electrodes to assemble flexible supercapacitors, which show a high gravimetric capacitance of 133 F/g [26]. Alignment of NFs by controlling the electrospinning parameters yielded a better electrical conductivity, higher surface area, and hence, a higher capacitance of 135 F/g [27]. To improve the electrical conductivity, Ag nanoparticle-decorated CNFs were prepared by electrospinning. The highest capacitance of 234.91 F/g was obtained for 5 wt% loading of Ag [24]. B_2O_3 was decorated in CNF to enhance the wettability and hence electrochemical performance. However, the maximum capacitance obtained with CNF-10 wt% B_2O_3 was only 126.31 F/g [28]. Therefore, there is an urgent need to develop strategies for designing CNFs. CNFs are naturally microporous; since double

†To whom correspondence should be addressed.
E-mail: kujie@naver.com, smjeong@chungbuk.ac.kr
‡Authors contributed the work equally.

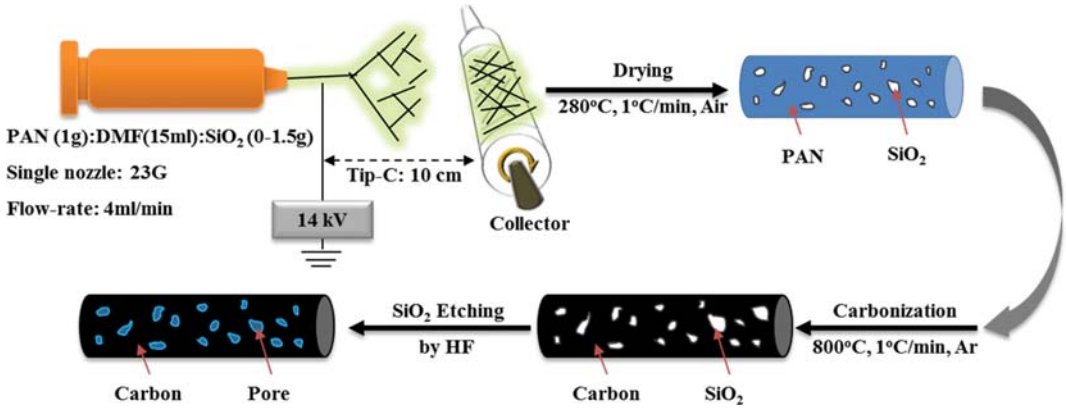

Scheme 1. Steps to fabricate porous CNF using the electrospinning method, subsequent annealing and etching step.

layer capacitance is primarily dependent on the surface area, it is crucial to increase the surface area of CNF electrodes. To access the interior of the nanotube, removal of the metal catalyst from the top of the carbon nanotube prepared by chemical vapor deposition has proven promising to improve the supercapacitive characteristics [29]. In particular, an open-ended carbon nanotube facilitates accessibility of electrolyte ions. Inspired by this, porosity was introduced in CNFs to increase their utilization in supercapacitor electrodes. This was achieved by preparing SiO_2-CNFs via electrospinning, followed by etching the SiO_2 nanoparticles [30]. However, a detailed investigation on the impact of SiO_2 nanoparticle loading and the subsequent porosity-dependent supercapacitive behavior of mesoporous CNFs has not been conducted thus far.

In this study, porous CNFs were prepared by electrospinning and subsequent selective etching. In addition to typical electrospinning, SiO_2 nanoparticles at different loading amounts were incorporated in an electrospun solution and selectively etched out to obtain porous CNFs. Notably, when used as a supercapacitor electrode in an aqueous electrolyte, the porous CNFs outperformed in terms of specific capacitance, cyclic stability, rate performance, and charge transfer kinetics compared to its pristine counterpart. This study provides a comprehensive insight into the effects of porosity, surface area, and physicochemical properties of porous CNFs on the supercapacitive characteristics. The strategy employed herein can enable the design of CNF-based electrodes with improved energy storage performance.

EXPERIMENTAL METHODS

1. Materials and Porous Carbon Nanofiber Preparation

Polyacrylonitrile (PAN, MW=150,000, Sigma-Aldrich) was used as the carbon precursor and *N, N*-dimethylformamide (DMF) was used as the solvent for preparing the PAN solution which was first prepared by dissolving 6 wt% of PAN powder in DMF stirred until clear and homogeneous. To obtain porous CNFs with different porosities, the SiO_2 nanoparticle content was varied from 0 to 10 wt%. The mixture was immediately placed in a plastic syringe fitted with stainless steel nozzle (23G) and the syringe was connected to an electrospinner (ESR100, NanoNC, Korea) for electrospinning. A voltage of 14 kV was applied between the nozzle tip to the collector distance of 10 cm and a flow rate of 4 ml/h. The electrospun SiO_2-CNFs were collected, and a two-step heating process was carried out. In the first step, the electrospun fibre was stabilized at 280 °C under an air atmosphere with a ramping rate of 1 °C/min. The temperature was then maintained at 800 °C for carbonization during the second step of annealing under Ar atmosphere. Thereafter, SiO_2 nanoparticles were etched from the surface of CNF by using 51% HF solution. At first, 10 ml HF was added in 40 ml H_2O and 0.2 g SiO_2 nanoparticle containing CNF was dipped in HF solution for overnight. To demonstrate the impact of porosity, pristine CNFs were prepared using a similar method without using SiO_2 nanoparticles in the electrospun solution (CNF). Other CNFs prepared from the electrospun solution after SiO_2 nanoparticle etching are labeled p-CNF-1, p-CNF-2, and p-CNF-3, in order of increasing porosity. The schematic for the preparation of porous carbon nanofiber is presented in Scheme 1.

2. Physical Characterization

Field-emission scanning electron microscopy (FESEM, Zeiss, ULTRA PRUS) was used to examine the morphology of the CNFs. The wetting nature of the fiber was examined by water contact angle measurements (GSM, Surfacetech Co., Ltd.). The crystal structure was determined by X-ray diffraction (XRD, D8 Discover with GADDS). To investigate the wettability, the electrode material was coated on a glass slab (as in the test for electrochemical performance), and 1 µl of water was used as the ambient environment. X-ray spectroscopy (XPS, Thermo Scientific, K-Alpha) was used to evaluate the chemical structure of the CNFs. To estimate the specific surface area, pore volume, and pore size distribution of the CNFs, N_2 adsorption/desorption isotherms were measured at 77 K by a surface area analyzer (Mastersizer 3000, Marvern). The Brunauer-Emmett-Teller (BET) method and the Barrett-Joyner-Halenda (BJH) model were used to estimate the specific surface area and pore size distribution, respectively.

3. Electrochemical Characterization

The electrochemical performance of the CNFs was evaluated in a standard three-electrode system using the AUTOLAB workstation (AUT84455). Graphite rods and Ag/AgCl (saturated in 3M KCl) were used as the counter and reference electrodes, respectively. A working electrode was prepared by mixing 80 wt% CNF as the active material, 10 wt% Super-P as the conductive additive, and

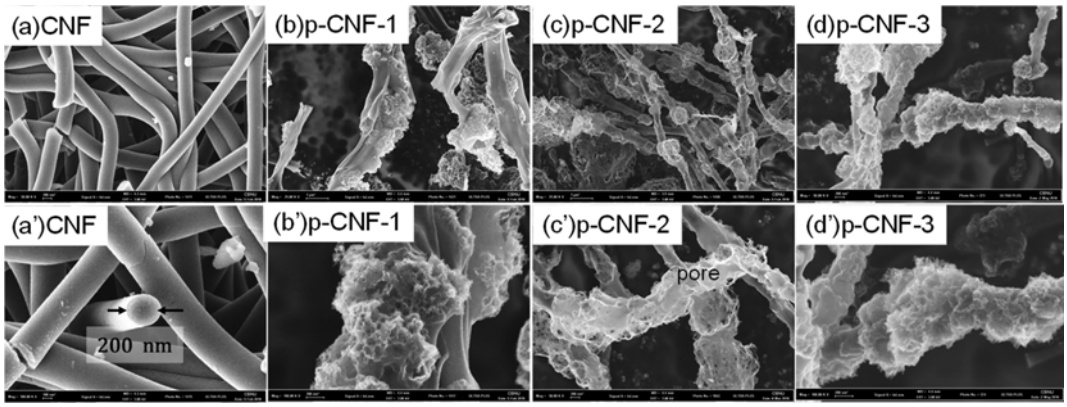

Fig. 1. Scanning electron micrographs of ((a), (a')) CNF, ((b), (b')) p-CNF-1, ((c), (c')) p-CNF-2, and ((d), (d')) p-CNF-3.

10 wt% polyvinylidene fluoride (PVDF) as the binder dispersed in *N*-methyl-2-pyrrolidone (NMP). The mixed slurry was uniformly coated on a Ti mesh and dried at 110° overnight. The loading amount of the CNF was varied from 1.6 to 2.4 mg/cm^2 over an area of 1 cm^2. The contribution from the Ti mesh was confirmed to be negligible before electrochemically testing the active materials. All electrodes were analyzed by cyclic voltammetry (CV) at scan rates of 5 to 100 mV/s, charge-discharge profiles at current densities of 1 to 20 A/g, and impedance spectroscopy with an alternating perturbation amplitude of 10 mV. Owing to its smaller protonic radius and higher ionic mobility, 1 M H_2SO_4 was used as the electrolyte [31,32]. The specific capacitance was estimated using the following relation [33]:

$$C=(I_d\times t_d)/(m\times V) \quad (1)$$

where C, I_d, t_d, m, and V are the specific capacitance, discharging current, the time taken to discharge, the mass of the active material, and operating potential window, respectively. The supercapacitor device was fabricated using two identical electrodes separated by a filter paper soaked with 1 M H_2SO_4 electrolyte. In the calculation of C of the symmetric device, the total mass of the electrodes was considered. The energy density (E) and power density (P) of the symmetric device were calculated by the following equations:

$$E=1/2\times C\times V^2 \quad (2)$$

$$P=E/t_d \quad (3)$$

RESULTS AND DISCUSSION

1. Morphological Analysis

The surface morphology of CNFs and p-CNF is shown in Fig. 1. The average diameter of CNF is found to be 200 nm and no porosity was found in the CNF surface as shown in the Fig. 1((a), (a')). Fig. 1((b)-(e')) shows p-CNF images. It is clearly evident the porosity is introduced along with the NF compared to bare CNF. Depending on the SiO_2 NP loading and followed by etching, the porosity and surface area will also increase. The quantitative details about pore diameter and surface area are evaluated by BET surface area measurement.

2. BET Analysis

The pore distribution and surface area are crucial to achieve high-performance double layer charge storage using a carbon nanostructure. Hence, the N_2 adsorption studies were carried out for all studied fibers; the results are shown in Fig. 2 and summarized in Table 1. CNF exhibited a specific surface area of 399 m^2/g. The surface area of p-CNF-1, p-CNF-2 and p-CNF-3 increased up to 403, 540, and 496 m^2/g, respectively. According to IUPAC classification, the adsorption isotherms of p-CNF-1, p-CNF-2, and p-CNF-3 are shown the type-IV in a pattern indicating co-existence of micropores and mesopores, and higher surface area compared to the CNF (type-II). The hysteresis loop was more prominent for relative pressure (P/P_0) in the range of 0.8-1 when the SiO_2 loading was

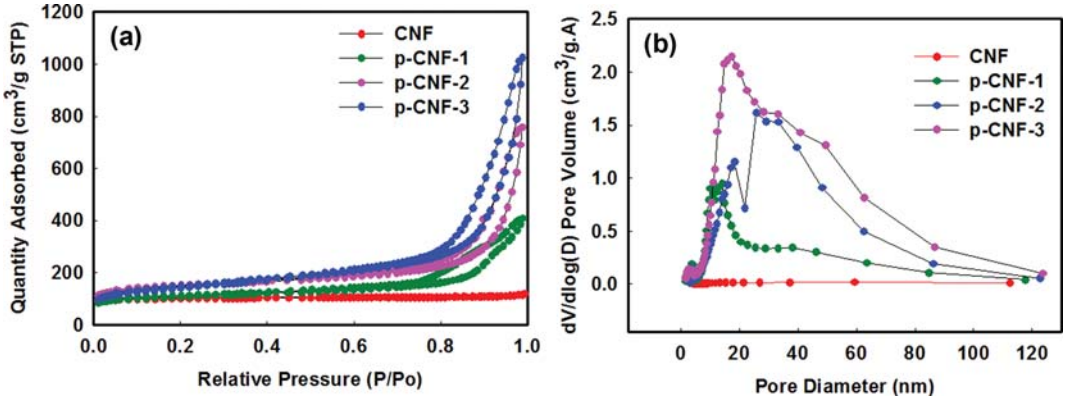

Fig. 2. (a) N_2 adsorption isotherms and (b) pore-size distribution of CNF and p-CNFs.

Table 1. Physico-chemical and electrochemical properties of CNF and p-CNFs

Samples	Physico-chemical properties						Sp. capacitance (F/g)
	Surface area (m^2/g)	Micropore fraction (%)	Avg. pore diameter (nm)	Avg. pore vol. (cm^3/g)	I_D/I_G	sp^2/sp^3	
CNF	399.09	97.85	5.13	0.03	1.75	1.89	107.11
p-CNF-1	403.42	67.70	13.47	0.52	1.40	2.25	183.00
p-CNF-2	540.27	65.90	18.10	1.03	1.31	2.54	207.00
p-CNF-3	496.51	38.97	17.45	1.49	1.04	3.21	247.78

increased and etched out (Fig. 2(a)). This implies the presence of a higher amount of micropores and mesopores in the structure. Hence, the micropore volume fraction for all CNFs was determined by BET measurement. Remarkably, the micropore volume decreased in the order of p-CNF-3 (38.97%)<p-CNF-2 (67.70%)< p-CNF-1 (65.90%)<CNF (97.85%). Eventually, the pore volume also increased from 0.03 to 1.5 cm^3/g for p-CNF-3. This signifies an increment in the mesoporous content for p-CNF-1, p-CNF-2 and p-CNF-3 with an average diameter of 14 to18 nm; the average diameter of CNF was 5 nm. Fig. 2(b) shows the pore diameter distribution of CNFs within 0-120 nm. p-CNF-3 has a large mesopore volume between 10 to 80 nm. Clearly, the as-synthesized CNF is mainly composed of micropores along the nanofiber as well as interconnected open space between the nanofibers. The additional porosity-induced p-CNF-1 and p-CNF-2 exhibit a hierarchical pore structure predominantly comprising mesopore, along with some mi-

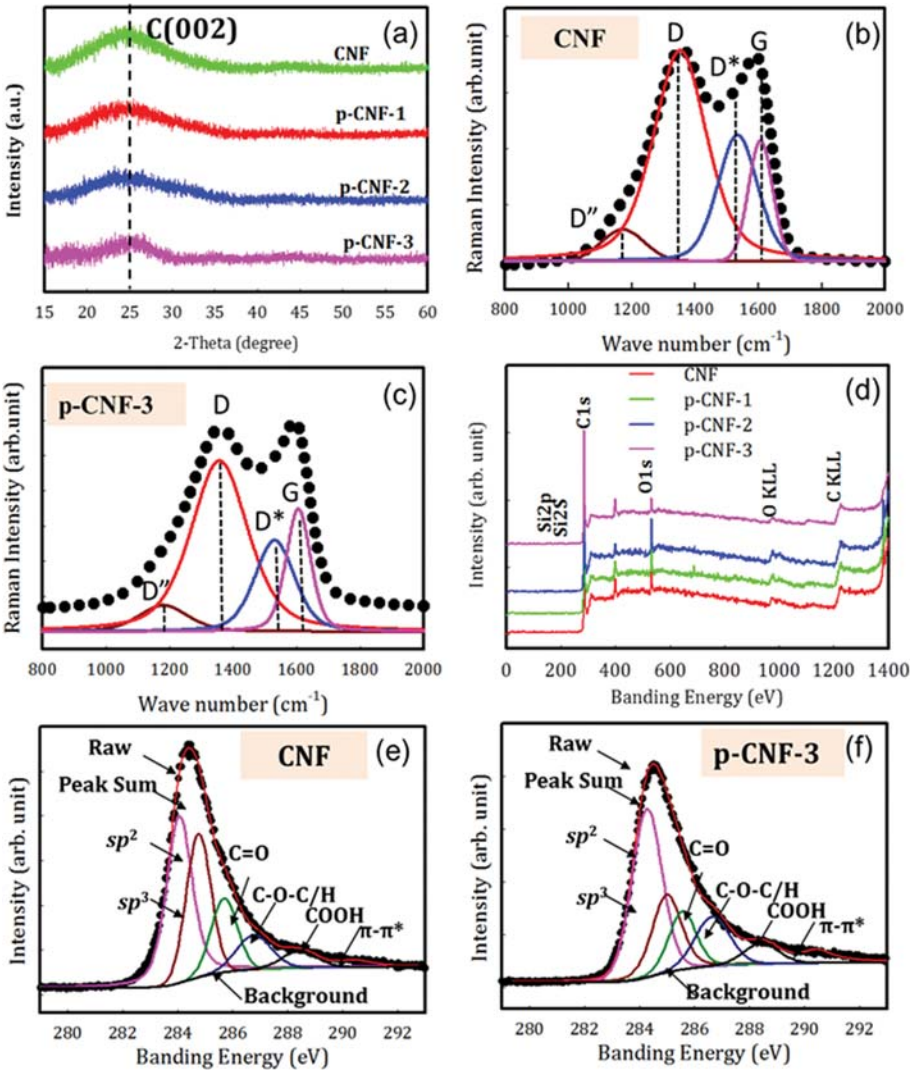

Fig. 3. (a) XRD pattern, ((b), (c)) Raman spectra, (d) XPS survey spectra of CNF and p-CNF, ((e), (f)) High-resolution C1s XPS spectra of CNF and p-CNF-3.

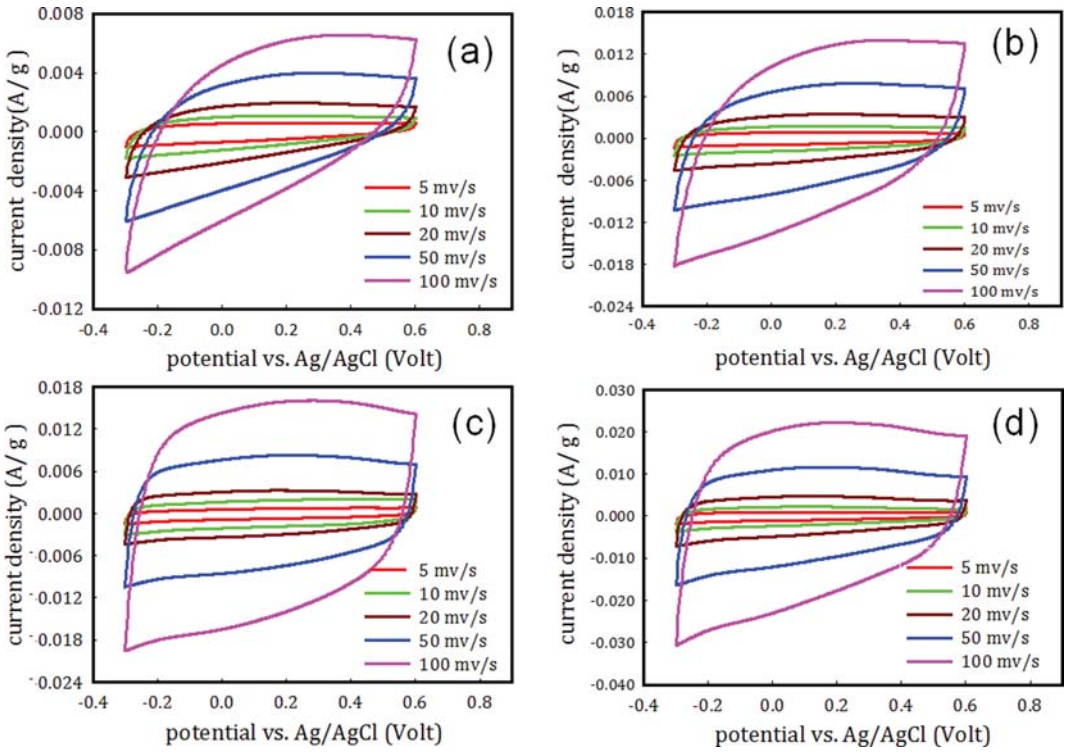

Fig. 4. Cyclic voltammogram of (a) CNF, (b) p-CNF-1, (c) p-CNF-2, and (d) p-CNF-3 at different scan rate.

cropores. These additional mesoporous-induced CNFs can improve electrode-electrolyte interactions and shorten the ionic transport paths, and hence promote the charge transport and accessibility for the electrolyte ion. The results herein demonstrate the successful pore engineering of CNFs using a pore expansion agent (SiO_2).

3. Structural Properties

The structural property of CNFs and p-CNFs was confirmed by the XRD patterns shown in Fig. 3(a). Two broad diffraction peaks observed at $2\theta=25^0$ can be indexed to the (002) crystal plane of graphitic carbon. To explore the graphitic structure of CNFs, the Raman spectra of CNF and p-CNF-3 are shown in Fig. 3((b), (c)). The Raman spectra are deconvoluted with four peaks [34,35]. The D band at 1,358 cm^{-1} and G-band at 1,598 cm^{-1} are the characteristics features of graphitic CNF. The additional peaks around 1,190 cm^{-1} (D″-band) and 1,510 cm^{-1} (D*-band) are assigned to the bond stretching modes of hydrogenated sp^3 carbon and interstitial defects or out-of-plane defects, respectively [34,35]. The intensity ratio of the D-to-G band (I_D/I_G) is the measure of crystallinity of carbon nanostructure. The I_D/I_G ratio of p-CNF-3 was found to be greater than that of CNF (Table 1). The drop in the I_D/I_G ratio indicates an improvement in the crystallinity of the structure. Notably, no Si peak is observed from the Raman spectra (Fig. 3(b), (c)), confirming the successful etching of SiO_2 nanoparticles from the surface. The XPS survey spectra of p-CNF-1, p-CNF-2 and p-CNF-3 (Fig. 3(d)) also confirm the complete etching of the SiO_2, thus agreeing with the Raman results. To further evaluate the composition, the high-resolution C1*s* XPS spectra of CNF and p-CNF-3 are shown in Fig. 3(e) and (f), and the XPS data was analyzed by a peak fitting program (PeakFit, Version 4, Jandel). The deconvoluted XPS spectra of C1*s* exhibit sp^2-C, sp^3-C, C=O, C-O-C/H, and COOH peaks. The peak with binding energy at 290 eV corresponds to the π-π* shake-up peak, indicating a graphitic structure [36]. To quantify, sp^2/sp^3 is estimated for the all samples. The sp^2/sp^3 ratio increased to 2.08 for p-CNF-3 in comparison to CNF (Table 1). The improved sp^2 content in p-CNF-3 agrees well with Raman spectroscopic results.

4. Supercapacitive Properties

The electrochemical performance of CNFs was evaluated using a three-electrode system. Fig. 4 shows the cyclic voltammogram (CV) at a scan rate of 5 to 100 mV/s in the 1 M H_2SO_4 electrolyte. The quasi-rectangular and mirror-symmetric shapes indicate excellent accessibility of electrolyte ion to the electrode material and ideal double-layer capacitive behaviour. The area under the CV curve was maximum for p-CNF-3; this is attributed to excellent charge storage due to more porosity and surface area. As shown in the CV curves at different scan rates, the persistence of the shape of the CV curve for all electrode materials without any degradation with sweep rate implies a decent capacitive behavior.

The electrochemical performance of CNFs obtained from CV is in good-agreement with the charge-discharge profile, as shown in Fig. 5. A near-triangular charge-discharge profile without significant potential drop was obtained for CNF and p-CNF. The specific capacitance of all studied samples is plotted in Fig. 5(e). The highest specific capacitance and rate capacitance of the p-CNF-3 are 247.78 F/g at 1 A/g and 73.54% once current density increased to 20 A/g, respectively. On the other hand, pristine CNF exhibits a specific capacitance of 107.11 F/g at 1 A/g and the capacitance decreases much faster, to 31.11 F/g at 20 A/g. Furthermore, the rate performance increases from 29.04% to 73.54%, while more porosity is introduced along the CNFs (Fig. 5(f)). The specific capacitance of studied electrodes is shown in Table 1. Excellent capacitive char-

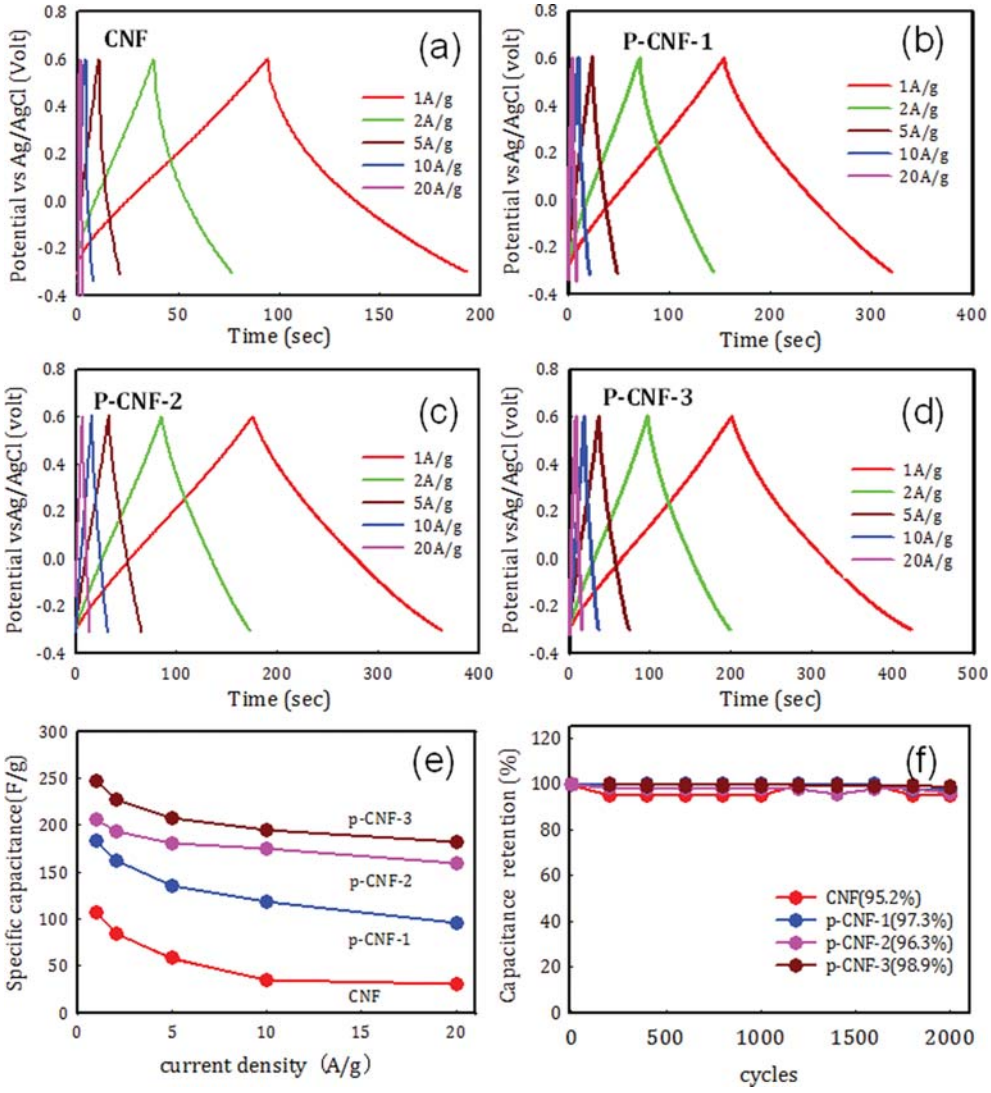

Fig. 5. Charge-discharge profile of (a) CNF, (b) p-CNF-1, (c) p-CNF-2, and (d) p-CNF-3 at different current densities, (e) specific capacitance versus current density and (f) cyclic stability of CNF and p-CNF.

Table 2. Comparison of supercapacitor performances of CNF with other reports

Material	Sp. capacitance (F/g)	Rate performance	Cycle stability	Ref.
CNF	60 at 1 mA/cm^2	73% 20 mA/cm^2		[38]
Aligned CNF	165 at 10 mV/s	67.3% at 50 mV/s		[27]
Graphene nanoplatelets-reinforced CNF	86.11 at 1 A/g	-	90%, 1000 cycles	[39]
Cross-linked N-doped CNF	223.8 at 0.5 A/g	78.5% at 50 A/g	106%, 20000 cycles	[40]
CNF/graphene	183 at 1 A/g	82.5% at 10 A/g	92%, 4500 cycles	[41]
N-doped CNF	242 at 0.2 A/g	72.7% at 2 A/g	99%, 5000 cycles	[30]
Hollow CNF/MnO_2	237 at 10 mV/s	97.3 F/g at 5 A/g		[42]
CNF-B_2O_3	126.31 at 1 mA/cm^2		91%, 3000 cycles	[28]
ZnO-activated CNF	178 at 1 mA/cm^2		75%, 1000 cycles	[18]
Metal ion-assisted acid corrosion P-CNF	104.5 at 0.2 A/g	56.5% at 10 A/g	94%, 2000 cycles	[25]
Double-capillary CNF	133 F/g at 1 A/g	74% at 20 A/g	94%, 10000 cycles	[26]
P-CNF-3	248 at 1 A/g	75.4% at 20 A/g	99 %, 2000 cycles	This work

acteristics were observed for p-CNF, compared to CNF. Moreover, the obtained specific capacitance of p-CNF-3 was higher than literature value for CNF (Table 2) and is impressive compared to those of carbon nanostructures (activated carbon, carbide-derived carbon,

carbon nanotube, graphene) [1,10,37]. The cycle performance of an electrode material is important for its use supercapacitor device. To investigate this, all studied materials were subjected to 2000 charge-discharge cycles at a current density of 1 A/g. Fig. 5(f) represents the cycle test of all samples. Approximately, 95.2, 97.3, 96.3, and 98.9% of the capacitance were retained after 2000 charge-dis-

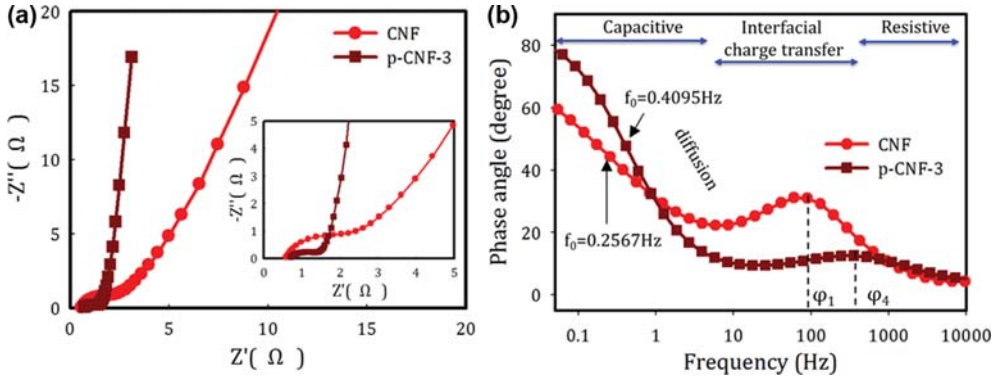

Fig. 6. (a) Nyquist plot and (b) Bode plot of the CNF and p-CNF-3 electrodes.

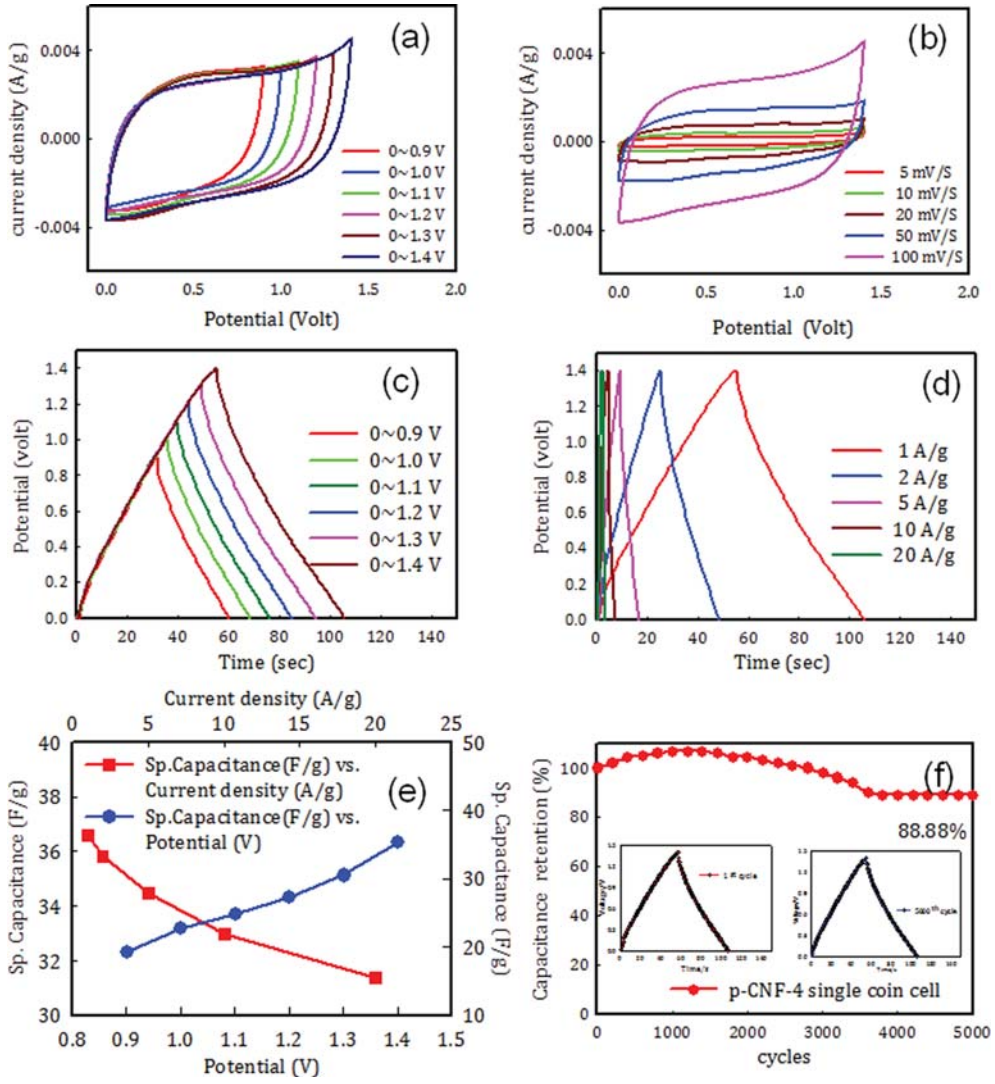

Fig. 7. Electrochemical performance of the symmetric device in 2-electrode by using the p-CNF-3 sample. Cyclic voltammogram at different (a) potential window and (b) scan rate. Charge-discharge profile at different (c) potential window and (d) current density. (e) Specific capacitance at the different current density and applied potential window and (f) cyclic stability.

charge cycles for CNF, p-CNF-1, p-CNF-2, and p-CNF-3, respectively. The high capacitance retention of p-CNF-3 demonstrates its potential as a supercapacitor electrode.

To further understand the electrochemical behavior of CNFs in terms of charge transfer kinetics, mass transport and diffusion kinetics, the impedance spectra of CNF and p-CNF-3 were thoroughly investigated with the help of Nyquist plot (Fig. 6(a)) and Bode plot (Fig. 6(b)). As depicted in Fig. 6(a), the Nyquist plot of p-CNF-3 was found to be steeper at lower frequency range compared to CNF, confirming the faster double layer formation. More significantly, p-CNF-3 shows lower radius semi-circle in high-frequency range compared to CNF, implying faster ion diffusion into the electrode. Fig. 6(b) shows the frequency dependent phase angle for all samples. The Bode plot is categorized into the capacitive, diffusive and resistive part in the low-frequency, mid-frequency and high-frequency range, respectively [17,43]. The maximum phase angle for the CNF and p-CNF-3 was 60° and 79°, respectively. Additionally, the characteristic frequency (f_0) at pa hase angle of 45° is obtained from Fig. 6(b) to find the time constant. The time constant ($\tau_0=1/f_0$) is the measure of faster charge-discharge response [44]. The lower time constant is found for p-CNF-3 (2.44 s) compared to CNF (3.89 s). In the mid-frequency range, all Bode plots show an additional peak. Interestingly, this peak (φ) shifted to higher-frequency region and intensity decreased for the sample p-CNF-3 (Fig. 6(b)). This fact reveals the lower charge-transfer resistance and reduction of ion diffusion resistance into the p-CNF-3 electrode compared to other studied electrodes [43,45].

In view of the practical utilization of CNF electrode material, a symmetric coin cell is fabricated out of p-CNF-3 electrode and H_2SO_4-soaked filter paper as separator-cum-electrolyte. The CV profile of the device, as shown in Fig. 7(a), reveals the ability to operate up to 1.4 V without any hydrogen and oxygen evolution. Fig. 7(b) shows the CV-profile of the device at various scan rates from 5 to 100 mV/s. The shape of the CV profile was found to be independent with the scan rate. This result indicates the excellent ionic transport and accessibility of full interior of the CNF. A similar result was also obtained from the charge-discharge profile at the different applied potential window and current density (Fig. 7(c)-(d)). The specific capacitance of the device was found to be 36.35 F/g while it operated at 1.4 V. The estimated specific capacitance with respect to the applied voltage and current density is plotted in Fig. 7(e). Additionally, the device shows excellent electrochemical stability up to 5000 cycles with only 11% capacitance fading (Fig. 7(f)). The obtained energy density for the single symmetric device is 9.9 Wh/kg with a power density of 0.69 kW/kg. Good controllability on the energy density and power density using tandem device empowers its utilization in practical applications.

CONCLUSIONS

A porous electrospun carbon nanofiber (p-CNF) was successfully designed via electrospinning method followed by subsequent etching of SiO_2 nanoparticles. The porosity and surface area of p-CNF were tuned by varying SiO_2 loading and hence its electrochemical performance. An improved capacitance, higher rate performance, only 1.2% capacitance fade after 2000 charge-discharge cycle and less charge-transfer resistance were exhibited by p-CNF in comparison with pristine one. The obtained result is inferred to increased mesoporous volume, high surface area, I_D/I_G ratio, sp^2/sp^3 ratio and less resistance of the additional porosity induced CNF. Thus, CNF preparation adopting the presented approach is expected to be a promising electrode material for energy storage devices.

ACKNOWLEDGEMENTS

This work was supported by the National Research Foundation of Korea (NRF) grant funded by the Korea government (MSIT) (2018R1A4A1024691) and by Basic Science Research Program through the National Research Foundation of Korea (NRF) funded by the Ministry of Education (2017R1D1A1B03031989).

REFERENCES

1. Z. Lin, E. Goikolea, A. Balducci, K. Naoi, P. L. Taberna, M. Salanne, G. Yushin and P. Simon, *Mater. Today*, **21**, 419 (2018).
2. B. E. Conway, Electrochemical supercapacitors : Scientific Fundamentals and Technological Applications, Kluwer Academic/Plenum Publishers (1999).
3. A. Borenstein, O. Hanna, R. Attias, S. Luski, T. Brousse and D. Aurbach, *J. Mater. Chem. A*, **5**, 12653 (2017).
4. L. Xia, L. Yu, D. Hu and G. Z. Chen, *Mater. Chem. Front.*, **1**, 584 (2017).
5. M. Inagaki, H. Konno and O. Tanaike, *J. Power Sources*, **195**, 7880 (2010).
6. S. Ghosh, S. M. Jeong and S. R. Polaki, *Korean J. Chem. Eng.*, **35**, 1389 (2018).
7. E. M. Jin, J. G. Lim and S. M. Jeong, *J. Ind. Eng. Chem.*, **54**, 421 (2017).
8. G. Sahoo, S. R. Polaki, S. Ghosh, N. G. Krishna and M. Kamruddin, *J. Power Sources*, **401**, 37 (2018).
9. S. Ghosh, S. R. Polaki, P. Ajikumar, N. G. Krishna and M. Kamruddin, *Indian J. Phys.*, **92**, 337 (2018).
10. C. Schütter, C. Ramirez-Castro, M. Oljaca, S. Passerini, M. Winter and A. Balducci, *J. Electrochem. Soc.*, **162**, A44 (2015).
11. N. R. Chodankar, S.-H. Ji and D.-H. Kim, *J. Electrochem. Soc.*, **165**, A2446 (2018).
12. S. Ghosh, G. Sahoo, S. R. Polaki, N. G. Krishna, M. Kamruddin and T. Mathews, *J. Appl. Phys.*, **122**, 214902 (2017).
13. X. Mao, T. A. Hatton and G. C. Rutledge, *Curr. Org. Chem.*, **17**, 1390 (2013).
14. A. Choudhury, B. Dey, S. S. Mahapatra, D.-W. Kim, K.-S. Yang and D. J. Yang, *Nanotechnology*, **29**, 165401 (2018).
15. N. Islam, M. N. Ferdous Hoque, Y. Zu, S. Wang and Z. Fan, *MRS Adv.*, **3**, 855 (2018).
16. C. Kim, K.-S. Yang and W.-J. Lee, *Electrochem. Solid-State Lett.*, **7**, A397 (2004).
17. E. Samuel, B. Joshi, H. S. Jo, Y. I. Kim, S. An, M. T. Swihart, J. M. Yun, K. H. Kim and S. S. Yoon, *Chem. Eng. J.*, **328**, 776 (2017).
18. C. H. Kim and B.-H. Kim, *J. Power Sources*, **274**, 512 (2015).
19. M. Cakici, R. R. Kakarla and F. Alonso-Marroquin, *Chem. Eng. J.*, **309**, 151 (2017).
20. W.-J. Lee, S. Jeong, H. Lee, B.-J. Kim, K.-H. An, Y.-K. Park and S.-C.

Jung, *Korean J. Chem. Eng.*, **34**, 2993 (2017).
21. I. Michio, Y. Ying and K. Feiyu, *Adv. Mater.*, **24**, 2547 (2012).
22. C. Kim and K. Yang, *Appl. Phys. Lett.*, **83**, 1216 (2003).
23. D.-D. Zhou, W.-Y. Li, X.-L. Dong, Y.-G. Wang, C.-X. Wang and Y.-Y. Xia, *J. Mater. Chem. A*, **1**, 8488 (2013).
24. S.-J. Park and S.-H. Im, *Bull. Korean Chem. Soc.*, **29**, 777 (2008).
25. Y. Liu, J. Zhou, L. Chen, P. Zhang, W. Fu, H. Zhao, Y. Ma, X. Pan, Z. Zhang, W. Han and E. Xie, *ACS Appl. Mater. Interfaces*, **7**, 23515 (2015).
26. J. Wang, J. Tang, Y. Xu, B. Ding, Z. Chang, Y. Wang, X. Hao, H. Dou, J. H. Kim, X. Zhang and Y. Yamauchi, *Nano Energy*, **28**, 232 (2016).
27. M. Kim, Y. Kim, K. M. Lee, S. Y. Jeong, E. Lee, S. H. Baeck and S. E. Shim, *Carbon*, **99**, 607 (2016).
28. J. H. Jeong and B.-H. Kim, *J. Taiwan Inst. Chem. Eng.*, **84**, 179 (2018).
29. Y.-S. Kim, K. Kumar, F. T. Fisher and E.-H. Yang, *Nanotechnology*, **23**, 015301 (2012).
30. L. Fan, L. Yang, X. Ni, J. Han, R. Guo and C. Zhang, *Carbon*, **107**, 629 (2016).
31. S. Ghosh, T. Mathews, B. Gupta, A. Das, N. G. Krishna and M. Kamruddin, *Nano-Struct. Nano-Objects*, **10**, 42 (2017).
32. E. Ismar, T. Karazehir, M. Ates and A. S. Sarac, *J. Appl. Polym. Sci.*, **135**, 45723 (2018).
33. M. D. Stoller and R. S. Ruoff, *Energy Environ. Sci.*, **3**, 1294 (2010).
34. R. Ding, H. Wu, M. Thunga, N. Bowler and M. R. Kessler, *Carbon*, **100**, 126 (2016).
35. S. Ghosh, K. Ganesan, S. Polaki, T. Mathews, S. Dhara, M. Kamruddin and A. Tyagi, *Appl. Surf. Sci.*, **349**, 576 (2015).
36. G. Sahoo, S. R. Polaki, S. Ghosh, N. G. Krishna, M. Kamruddin and K. Ostrikov, *Energy Storage Mater.*, **14**, 297 (2018).
37. S. Ghosh, S. R. Polaki, M. Kamruddin, S. M. Jeong and K. K. Ostrikov, *J. Phys. D: Appl. Phys.*, **51**, 145303 (2018).
38. B.-H. Kim and K. S. Yang, *J. Ind. Eng. Chem.*, **20**, 3474 (2014).
39. W. K. Chee, H. N. Lim, Z. Zainal, I. Harrison, Y. Andou, N. M. Huang, M. Altarawneh and Z. T. Jiang, *Mater. Lett.*, **199**, 200 (2017).
40. Y. Cheng, L. Huang, X. Xiao, B. Yao, L. Yuan, T. Li, Z. Hu, B. Wang, J. Wan and J. Zhou, *Nano Energy*, **15**, 66 (2015).
41. Q. Dong, G. Wang, H. Hu, J. Yang, B. Qian, Z. Ling and J. Qiu, *J. Power Sources*, **243**, 350 (2013).
42. S. Hong, S. Lee and U. Paik, *Electrochim. Acta*, **141**, 39 (2014).
43. A. Eftekhari, *J. Mater. Chem. A*, **6**, 2866 (2018).
44. J. Cai, H. Niu, H. Wang, H. Shao, J. Fang, J. He, H. Xiong, C. Ma and T. Lin, *J. Power Sources*, **324**, 302 (2016).
45. K. V. Sankar and R. K. Selvan, *RSC Adv.*, **4**, 17555 (2014).